Crack propagation in filled elastomers: 3D study of mechanisms involving the filler agglomerates

Jesbeer Kallungal, Laurent Chazeau, Jean-Marc Chenal, Jérôme Adrien, E Maire, Claire Barrès, Bernard Cantaloube, Patrick Heuillet, Fabian Wilde, Julian Moosmann, et al.

Crack propagation in filled elastomers: 3D study of mechanisms involving the filler agglomerates

Jesbeer. Kallungal[1,2,3,*], Laurent. Chazeau[1,*], Jean-Marc. Chenal[1], Jérôme. Adrien[1], Eric. Maire[1], Claire. Barrès[2], Bernard. Cantaloube[3], Patrick. Heuillet[3], Fabian Wilde[4], Julian Moosmann[4], Timm Weitkamp[5]

[1]*Univ Lyon, INSA Lyon, CNRS, MATEIS UMR5510, F-69621, Lyon, France*

[2]*Univ Lyon, INSA Lyon, CNRS, IMP UMR5223, F-69621, Lyon, France*

[3]*LRCCP, F-94408 Vitry-sur-Seine, France*

[4]*Helmholtz-Zentrum Hereon, Max Planck Strasse, 21502 Geesthacht, Germany*

[5]*Synchrotron SOLEIL, F-91190 Saint-Aubin, France*

Corresponding authors: laurent.chazeau@insa-lyon.fr

ABSTRACT

This paper presents the impact of Carbon Blacks agglomerates, at different concentrations, on crack propagation mechanisms in a Carbon black (CB) filled Ethylene Propylene Diene Monomer (EPDM) elastomer. As shown by Transmission electron microscopy, these CB agglomerates (CB_{aggl}) consist of aggregates clusters with interpenetrating elastomer, and for this reason, are soft and deformable. Crack tip observation using X-ray tomography demonstrates that these CB_{aggl} can either undergo fracture or arrest/ deviate a crack during its propagation. This causes higher energy dissipation at the crack tip, which contributes to the dissipative component of the strain energy release rate G. For this reason, it is found that among the two materials tested with a significant amount of CB_{aggl} (more than 3%), the material with the highest concentration has a slower crack propagation speed at high G.

1. INTRODUCTION

Many applications such as tyres, sealants, and anti-vibration device uses elastomer based materials. In these applications, these materials undergo static or dynamic strain

solicitations which reduce their durability. They contain reinforcing fillers such as carbon black (CB), silica nanoparticles, clay, talc or carbon nanotubes to improve their ultimate, fatigue and/or visco-elastic properties[1,2]. These fillers can form micron sized agglomerates (created by the agglomeration of nanometric sized filler aggregates) in the processed materials, in spite of the efforts made to avoid what is considered as defects or flaws[3,4]. Other defects can also be found like metallic oxides inclusions, micro-bubbles or voids. Unfortunately, all these defects are known to influence the rupture properties.

Since 1950s, many researchers extensively studied these properties in rubber materials. Rupture is the consequence of the initiation and propagation of a crack or multiple cracks through the entire section of the material, for instance, during fatigue [5–7] monotonic cycle[8] or quasi-static[9,10] solicitation. In some cases, crack propagation mostly dictates the durability of the material. Hence, many studies characterized the material evolution in the vicinity of a crack tip during the crack growth during fatigue [11–15] or quasi-static solicitation[16]. Postmortem analysis using electron microscopy showed the presence of defects like ZnO, carbon black agglomerates (CB_{aggl}), and cavities in the crack vicinity[11–15]. The high hydrostatic stress beyond the crack tip promotes the formation of cavities at the poles of the defects[9,11,16,17]. These cavities participate in the crack propagation which occurs by successive breaking of material ligaments around them [12,18]. On the other hand, in the case of filled elastomer, improvement of resistance to crack propagation is ascribed to the ability of the filler to deviate or arrest the crack[19]. Crack can follow the contours of the fillers, increasing the crack path length[20]. Same mechanisms are also suspected for filler agglomerates, but they have not been explored. It was also shown that the crack can also be arrested by the reinforced anisotropic structures (fibrillary structure) formed at the crack tip where the material is submitted to very large strain[21]. Even though all these mechanisms are often discussed in literature, their experimental observation is much less reported, especially using in situ techniques.

Various tools such as Scanning electron microscopy (SEM), Transmission electron microscopy (TEM), Atomic Force Microscopy, Small Angle X-ray Scattering, and X-ray Tomography are available to precisely characterize the defects in elastomer materials. Although techniques like SEM[14,22,23], TEM[24] and AFM[25] provide a better resolution, use of these techniques for in-situ characterization is limited due to small observable area, small size of the sample, or to the material degradation during the observation. SAXS is a non-destructive characterization technique that provides spatially averaged information at sub-micron scale such as the average particle size, shape, distribution of defects or cavities[26]. It is however

difficult to visualize or quantify the local dissipative mechanisms occurring in the crack tip vicinity using this technique. Recent studies showed that X-ray tomography using laboratory or synchrotron sources is a powerful technique which can provide 3 dimensional information of the microstructures inside the sample at the micron-scale[27–29]. This technique is also suitable to conduct in-situ analysis[30] on the crack propagation and to characterize the materials, crack surface and material evolution in the vicinity of the crack notch.

Thus this paper aims at understanding the impact of defects, specifically CB_{aggl} on the crack propagation in elastomer materials. The influence of the defects concentration will be explored, thanks to the study of model materials with different CB_{aggl} concentrations. It will be shown that the difference in the crack propagation resistance correlates with the energy dissipation inside the material, which is related to these agglomerates concentration. In addition, In-situ tensile and crack propagation tests using X-ray Tomography will enable to understand the various mechanisms associated to the agglomerates and at the origin of this dissipation energy.

2. MATERIALS AND TESTING

2.1 Composition and materials processing

Model materials used for the current study are based on a non-crystallizing Ethylene Propylene Diene Monomer Rubber (EPDM Keltan 4450) reinforced with high furnace carbon black (N326 from Cabbot) and cross-linked using unsupported Bis (α,α-dimethylbenzyl) peroxide. The composition of the model materials (Table 1) was kept constant whereas compounding process conditions were varied in order to generate more or less flaws inside the materials. All the ingredients except the peroxide were mixed in a Haake Rheomix 600 OS mixer (chamber volume: 120cm^3) using Banbury rotors (42 cm^3) at a given rotor speed and with a given mixing time (Table 1), and were then passed 10 times in a two-roll mill where the peroxide was added. The sequence of ingredients addition is detailed in Table 1. USD method refers to “upside down”, i.e., the elastomer was added after carbon black and TD method refers to “top down”, i.e., carbon black was introduced after the elastomer in the internal mixer. After the mixing steps, the samples were molded into plane strain geometry (PS) specimens[31] (Length=35mm, height =5mm, width =0.8mm, this geometry being also called Pure Shear geometry in some publications) by hot pressing at 170°C under 190 MPa for 12 min. Curing time was estimated from torque measurements performed using a Monsanto rheometer analyzer.

Table 1: Composition of the model materials

Ingredients	F1	F2	F3
	(Phr)	(Phr)	(Phr)
EPDM Keltan 4450	100	100	100
Carbon Black N326	50	50	50
Peroxide	3.2	3.2	3.2
Rotor Speed (rpm)	30	60	60
Mixing Time (min)	2	4	10
Introduction Protocol	TD 1.EPDM 2.CB	USD 1.CB 2.EPDM	TD 1.EPDM 2.CB
Filler Volume Fraction	19.3%	19.3%	19.3%

2.2 Multiscale characterization of materials

Microstructural analysis was performed using X-ray Tomography (laboratory source and synchrotron radiation source). The internal structure of carbon black agglomerates or aggregates was characterized by TEM.

2.2.1 X-ray tomography laboratory source (Lab Tomography):

The laboratory X-ray tomography device, used for postmortem analysis of the crack propagation path and to characterize the fracture surface, is the EasyTom apparatus from RX Solutions. The Tungsten target current is 45 µA. LaB_6 cathode filament is used, along with a CCD detector. The volume analyzed is ca. 4-8mm^3 with a voxel resolution chosen in the range of 1-2μm^3 depending on the requirements. The sample was rotated over 360° by steps of 0.09° in front of the X-ray beam. The tube voltage was kept at 40kV to have an optimised attenuation contrast between the elastomer and the agglomerates[32]. Each projection step required 0.45 s and the total time per scan was 30 minutes.

2.2.2 Synchrotron radiation computed tomography (SRCT)

SRCT experiments were performed with the PETRA III P05 beamline at DESY, Germany (operated by Helmholtz-Zentrum Hereon), and the Anatomix beamline at SOLEIL, France. The P05 beamline was used to study the local damage mechanisms inside the material during a tensile test. The monochromatic X-rays energy was fixed at 15keV with a spatial resolution of 2.19µm. The sample was mounted in a tensile rig (Figure 1a). Its specific geometry (Figure 1b)

was designed to create higher stress in the region of interest (ROI). The sample was rotated over 360° by steps of 0.225°. Each projection step lasted 30ms per projection resulting in a total time per scan of 50s. Experiments performed at Anatomix @SOLEIL [33] focused on the phenomena occurring beyond the crack tip during quasi-static uniaxial extension. The filtered white beam used had a mean energy of 20keV. The experimental setup is shown in Figure 1c. The spatial resolution was 1.3µm. The sample was rotated over 360° by steps of 0.18°. Each projection required 150 ms resulting in a total time per scan of 360s. The Pagnanin algorithm was applied to reconstruct the phase inside the sample[34]. Similar filter was not used with the data obtained with the P05 beamline, as 3D reconstruction was performed from attenuation contrast.

2.2.3 Transmission electron microscopy (TEM)

Nanoscale characterization was performed using TEM (CM120 Philips microscope) on a section with 90nm thickness prepared by cryo-ultra-microtomy (Leica Ultra cut UCT microtome). This section is placed on a 400-mesh copper grid. The accelerating voltage was set to 120kV and the CCD detector used is an Orius CCD camera from Gatan.

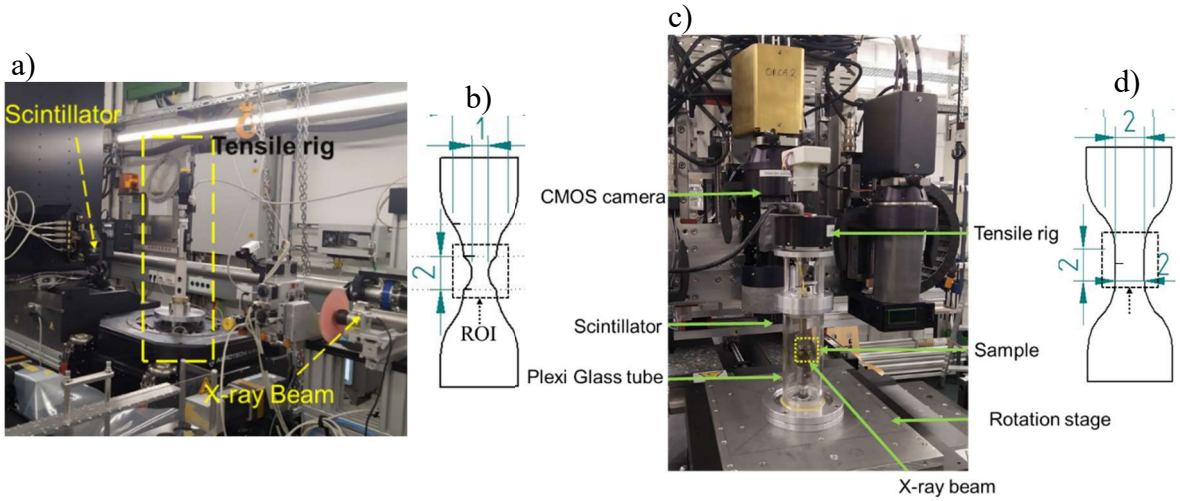

Figure 1: P05 beamline experiments: a) general view of the setup with the position of X-ray beam, tensile rig and scintillator, b) sample geometry used for in-situ tensile test. Anatomix beamline: c) homemade tensile rig from MATEIS lab, d) Single edged notched sample geometry used for in-situ crack propagation test.

2.3 Mechanical testing

2.3.1 Tensile test

Tensile tests were conducted on an MTS 1/ME machine equipped with 1kN load cell to obtain nominal stress-strain curves. The nominal stress is defined as $\sigma_n = F(t)/S_0$, where F is the force and S_0 is the initial section of the sample. The nominal strain is defined as $\epsilon_n = \frac{\Delta L}{L_0}$, where ΔL is the sample displacement and L_0 is the initial length. The fixed crosshead speed was 1mm/min, corresponding to an initial strain rate of 0.0065 s^{-1}.

2.3.2 Dynamic mechanical analysis

DMA Q800 (TA Instruments) was used to study the viscoelastic behavior of the materials. Dynamic strain sweeps tests were performed in shear sandwich mode at 30°C and 1 Hz in the shear strain range [0.01% - 10%].

2.4 Crack growth measurement technique

2.4.1 Strain energy release rate versus crack propagation speed

Crack propagation speed (Vp) was characterized as a function of the strain energy release rate. G is the product of $W(\lambda)$ by h_0 for a PS geometry specimen with a crack displacement length c, where $W(\lambda)$ is the strain energy density of the unnotched sample submitted to a stretching of λ with an initial height of h_0 [35]. $W(\lambda)$ is calculated from the area under the curve of the nominal stress- nominal strain plot. This one is obtained from the tensile test of unnotched PS specimen, using Digital Image Correlation (combined with the CORELI software, with image acquisition frequency was 1Hz). The DIC resolution is estimated to be 34 μm.

We applied a modified version of the static-growth test introduced by Lake *et al.* [36] involving the continuous deformation of a notched test piece (PS) at a constant strain rate (0.0065 s^{-1}). This allows to characterize Vp over a broad range of strain energy release rate. Note that the samples were not accommodated prior to the crack propagation test. An initial notch (c_0) of 10mm was made on one side of the test piece with a thin razor blade. Crack displacement up to 5 mm was considered for the analysis of Vp, to ensure conditions required by Yeoh *et al.* [37], i.e., $1.25 < c/h_0 < 3$ ($c=10$mm, $h_0=5$mm). The acquisition of the crack images during the first 90s of crack propagation test was performed every 100ms (crack propagation is slow), the time intervals was reduced to 10ms for the rest of the experiment. For that we used high speed camera enabling image acquisition up to 200hz.

Crack contour (Figure 2a, b, c) and displacement (Figure 2d) were derived from every image using ImageJ © free software and python modules [38]. To obtain a Vp(G) curve, Vp was calculated for every 0.2 kJ/m^2 G variation from the equation $Vp = c_{G+0.2} - c_G / \Delta t$, where c refers to crack tip position (Figure 2b). Finally, the averaged Vp of 3 specimens of the same material was used for plotting the Vp(G) curves. In addition, an "instantaneous" crack speed (V_{pi}) was calculated from the crack displacement between two consecutive images, plotted as a function of the G corresponding to the material strain when the second image is taken.

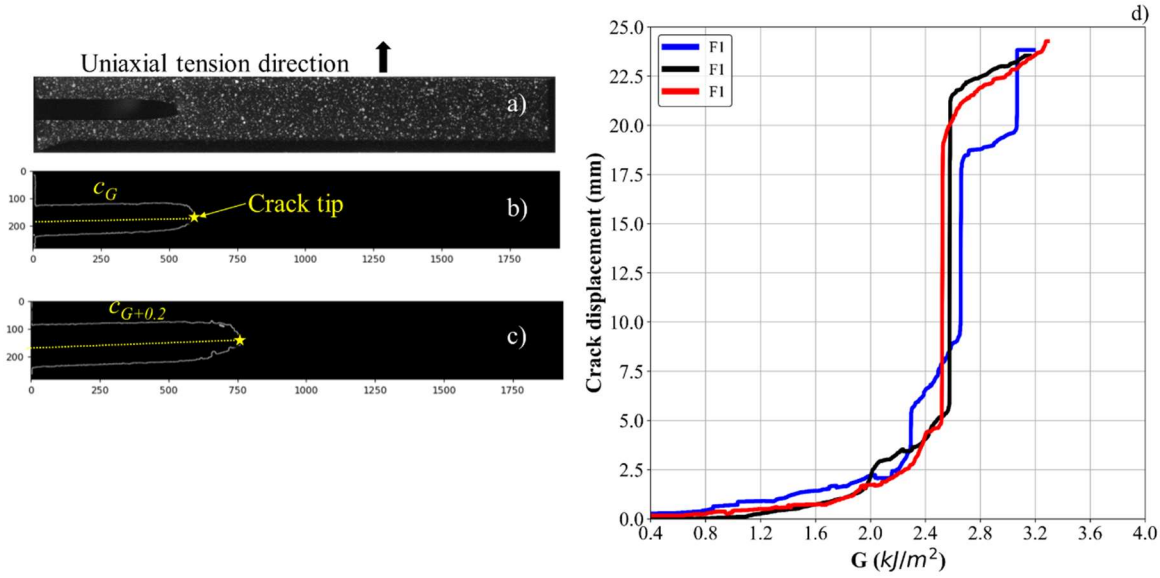

Figure 2: a) Stretched notched PS specimen with speckled pattern. b) Crack contour plotted derived from the picture (a) at a given G. The yellow star denotes the crack tip c) evolution of the crack contour after the increase of G by 0.2kJ/m^2. d) Crack displacement measured with three specimens of the same model material F1 as a function of G. The same plots for F2 and F3 materials are reported in SI (Figure A1).

2.4.2 In-situ crack propagation test using X-ray tomography (Anatomix)

For the in-situ tomography study of the crack propagation, single edge notched geometry (SENT) (Figure 1d) was used instead of PS geometry due to field of view limitations (2.3mm x 2.3mm x 2.3mm). The notched sample was stretched up to a given strain (10%, 20% 30% etc.) and maintained at this stretching level for 20 min during which the crack can propagate. To stop the crack propagation and the material movements during the tomographic scan, the sample deformation was decreased by 2.5% before launching the 8 min scan. This protocol enables to obtain images with good quality.

3. RESULTS

3.1 Multiscale CB_{aggl} analysis

Lab Tomography was used for the characterization of the CB_{aggl} existing in the different model materials[32]. The cumulative volume fraction (ϕ_{cumul}) of CB_{aggl} whose volume is above 125µm^3 is 10.1%, 3.0% and <0.2% in F1, F2, and F3, respectively (in the following, CB_{aggl} will implicitly refer to these agglomerates with volume larger than 125µm^3). Similar characterization of micron size agglomerates using synchrotron radiation computed Tomography (SRCT) leads to slightly higher values (11.5%, 4.3% and <0.85% in F1, F2, and F3 respectively), due to a better detection of CB_{aggl} . Since good correlation is observed between both methods and more data are available from lab tomography, ϕ_{cumul} calculated from this technique will be quoted throughout this paper. F1 has a higher percentage of agglomerates with intermediate and big size (Figure A2 in SI). Eq_{diam} represents the diameter of a fictive inclusion having the same volume as the analyzed CB_{aggl}. The mean size (i.e. mean Eq_{diam} value) of the CB_{aggl} in F1, F2 and F3 is 10.8µm, 11.0 µm and 9.7µm respectively. Based on the ϕ_{cumul}, F2 can be considered as more representative of industrial grade rubber compounds and F3 as a special case which rarely exists in the industry.

As shown in the TEM image in Figure 3, CB_{aggl} detected by tomography are actually made of local overconcentration of aggregates (of nanometer size,with an equivalent diameter in the range of 100 nm) inter-penetrated by elastomer. At 200nm resolution, we can observe the dispersion of aggregates either in CB_{aggl} or in the matrix of F1 (Figure 3b). Thus, the detected agglomerates appear as soft deformable clusters in which concentration of aggregates varies locally.

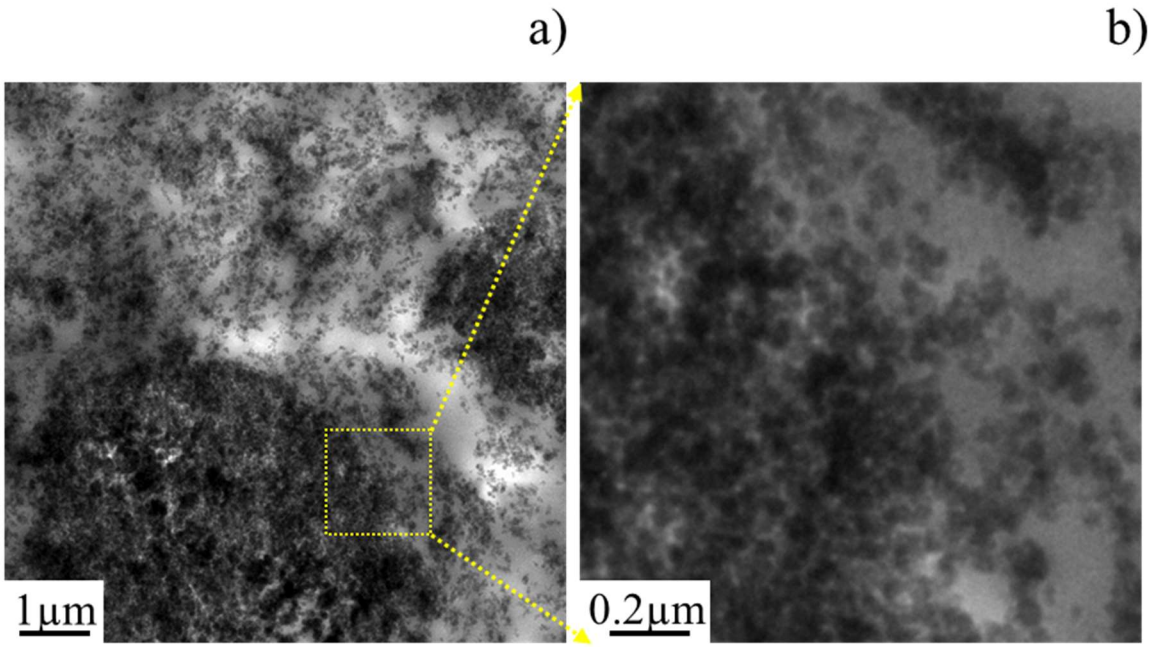

Figure 3: a) TEM image of a slice of CB_{aggl} in F1 at a resolution of 1µm, b) zoomed portion of the yellow square in 'a)' at a resolution of 200nm.

3.2 Macroscopic properties

3.2.1 Dynamic and mechanical properties

The dynamic mechanical analysis (at 1Hz & 30°C) shows that all the model materials have similar dynamic properties for deformation below 8% (Figure 4a). The viscoelastic properties of the materials are governed by the size of the filler aggregates, their volume fraction, and the polymer-filler interactions. Nevertheless, the variation of the agglomerates concentration from 0 to 10.1% does not have a significant impact here. This can be explained by the nature of the agglomerates which are made of aggregates in strong interactions with polymer chains. The concentration of agglomerates does not seem either to have a significant impact on the mechanical properties measured during a monotonic uniaxial loading test (PS geometry: Figure 4b). All the materials show a similar stress strain curve up to to 100% strain (it was also checked for dogbone geometry).

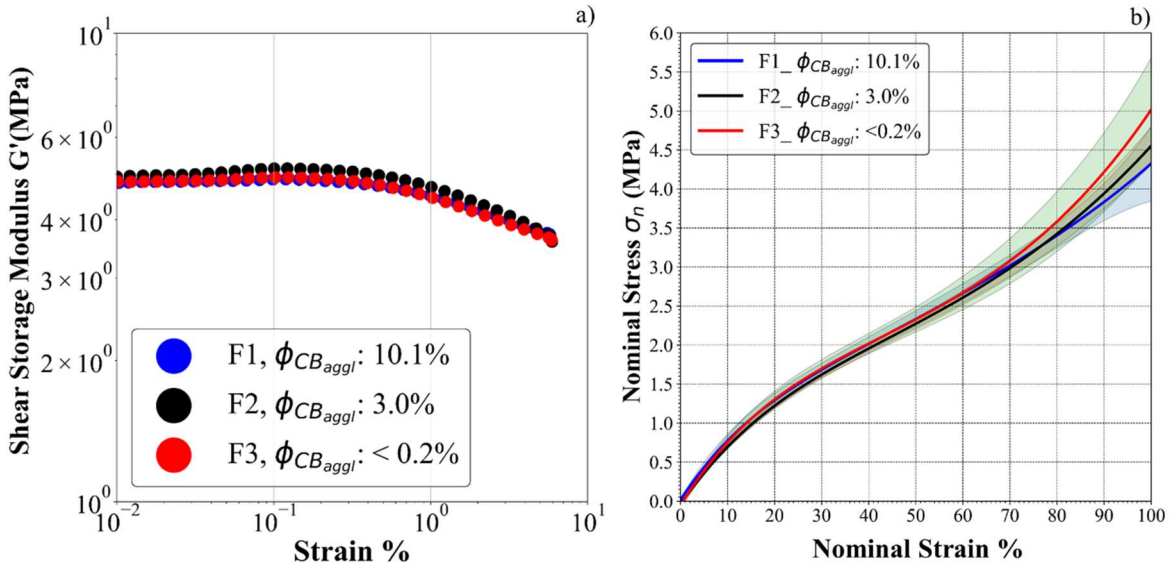

Figure 4 a) Shear storage modulus vs strain sweep for 3 model materials, b) Nominal stress vs nominal strain properties up to 100% strain of model materials using unnotched PS geometry. The shaded region along each curve represents the standard deviation. True Stress vs nominal strain properties up to rupture are given in SI (Figure A3).

The materials have been cyclically strained three times up to a fixed nominal strain (25%, 50%, and 75%) using a dogbone sample geometry (Figure 1d). For a given maximum nominal strain, the unloading curves of the three cycles superimpose while the loading curves for the 2nd and 3rd cycle coincide with each other and are below the 1st loading curve (Figure A4 in SI). Such behavior is observed with filled elastomer and is characteristic of the so-called Mullins effect. The energy dissipated only during the first cycle[39] is deduced from: $\Delta U^n_{hys} = \int_{0\ cycle\ 1}^{\epsilon_{\max\_mullins}} \sigma_N d\epsilon - \int_{0\ mean(cycle\ 2\ \&3)}^{\epsilon_{\max\_mullins}} \sigma_N d\epsilon$, where σ_N and ϵ are the nominal stress and strain and $\epsilon_{\max\_mullins}$ is the maximum nominal strain applied during the cycle. The hysteresis loss (ΔU^n_{hyst}) at high strain is higher for F1 (Figure 5) compared to F2 and F3.

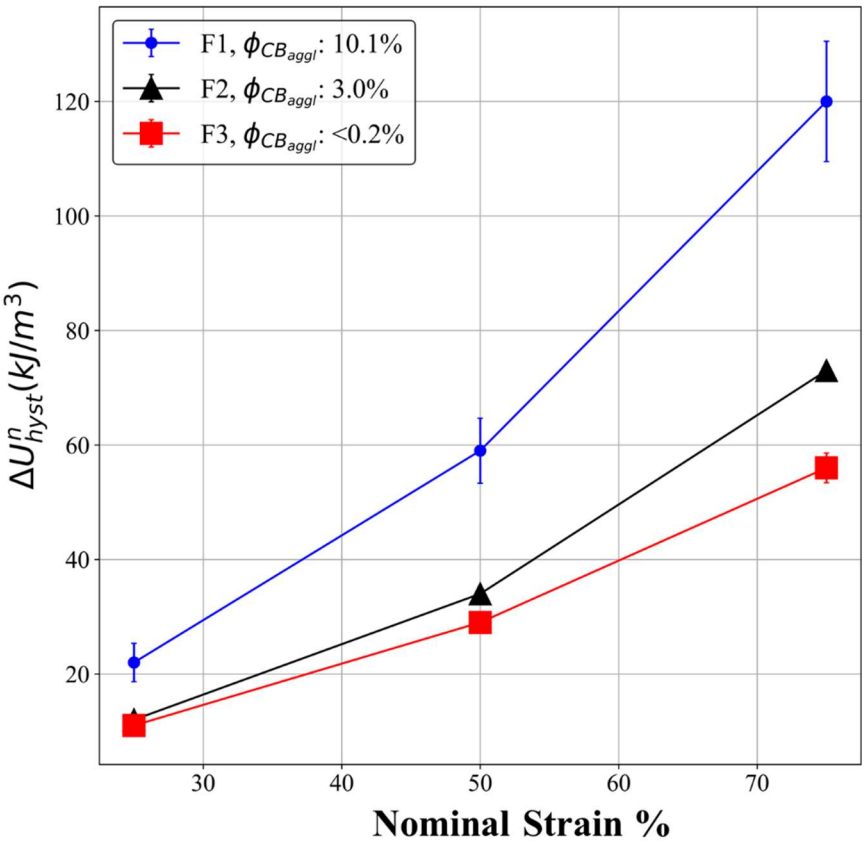

Figure 5: Irreversible hysteresis loss (ΔU^n_{hyst}) for F1, F2 and F3.

3.2.2 Crack propagation regime

Figure 6 presents the "*instantaneous*" crack speed measured during a continuous uniaxial deformation of a notched PS sample. At G below 2kJ/m2, the acquisition frequency is high enough so that the crack displacement is close to the resolution limit of the camera (10 microns), which explains why the deduced V_{pi} is either nul or constant. In F1 and F2 materials, the irregular alternance of these values suggests that the crack propagates by several sequences of growth and arrest, rather than a continuous propagation, for G value below 1.2kJ/m^2 for F1 and ca. 0.8-1.2 kJ/m^2 for F2. For F3, the results indicate a rather continuous crack propagation for all the G measurement domain (Figure 6c). This is consistent with observations of the crack surface of the ruptured materials. Figures 6 d-f presents the crack surface projection on a 2D projection plane. The color coding is the height variation of crack surface (Z profile) with respect to the Z value at the origin of the crack. The typical characteristics of stick slip crack surface shape such as saw tooth[21], wavy[16], etc. can be observed in Figures 6 d-f. This appears as a linear or triangle-shape wave front. All these results confirm that Vp is in the

domain of the Vp(G) curve where stick slip occurs [16,18,21,40]. Occurrence of crack arrest is more frequent in F1 (higher number of triangle wave front). The number of crack arrests for F2 is intermediate between F1 and F3. In F3, the crack propagation leads to a rather smooth profile.

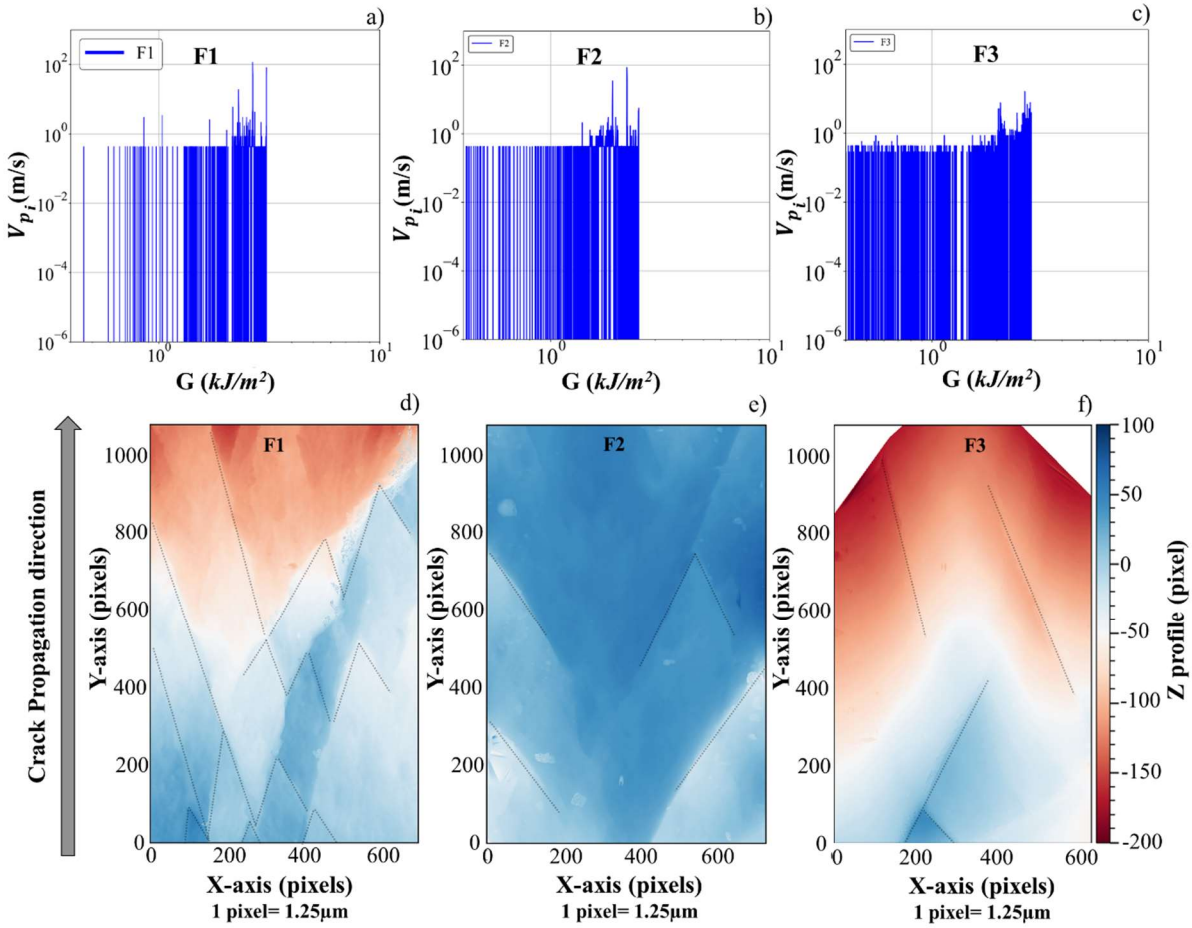

Figure 6 a), b), and c): Examples of instantaneous" crack speed (V_{pi}) calculated from the crack displacement between two consecutive images acquired during the uniaxial test for the model materials F1, F2, and F3, respectively using notched PS sample geometry. Each line represents a sequence of crack growth and arrest (see experimental details in section 2.4.1). Crack growth is continuous within the image acquisition time when there is no white space between consecutive lines. d), e) and f) crack surface for the model materials F1, F2, and F3, respectively. The color range indicates the height variation with respect to the height of the initial crack. The pixel resolution is 1.25µm

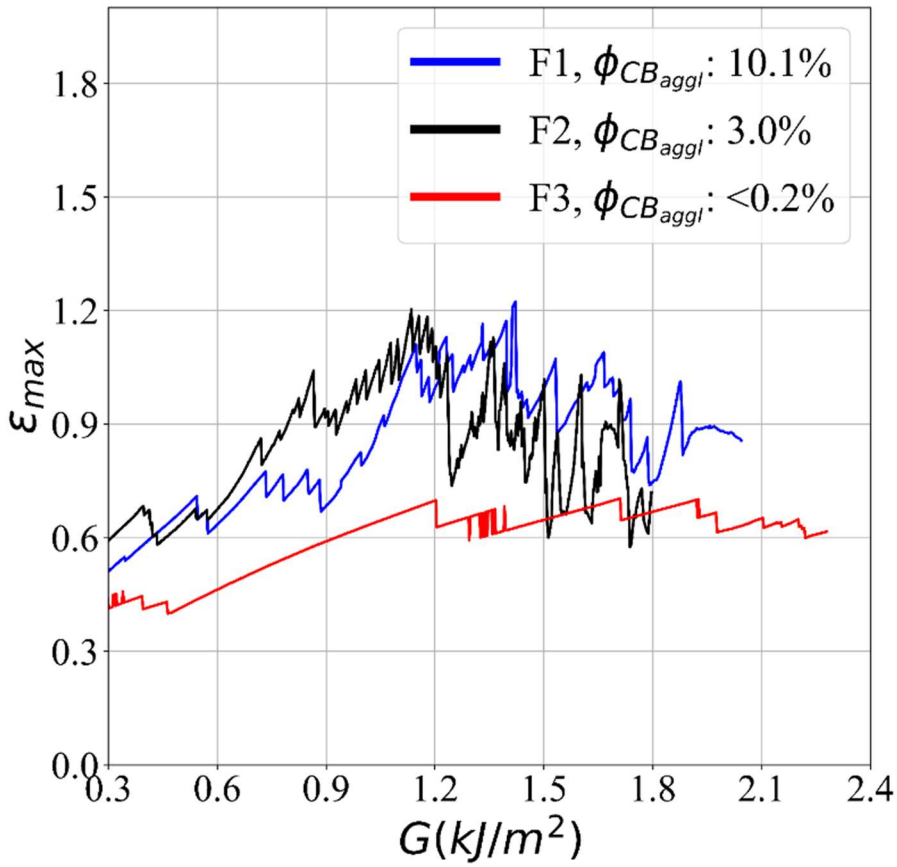

Figure 7: ϵ_{max} observed next to crack tip as a function of G for F1, F2 and F3,

The displacement field was deduced from the images acquired during the crack propagation (cf. SI Figure A5). From this, the nominal strain in the tensile direction was calculated as a function of the distance to the crack tip, for different G. The nominal strain (in the tensile direction) at the crack tip is maximal and noted ϵ_{max}. As shown in Figure 7, ϵ_{max} is above 50% for F1 and F2 for any given G. The zig-zag pattern in the maximum nominal strain curve confirms the existence of cycles of crack growth and arrest during the crack propagation. As expected, the ϵ_{max} profile for F3 is much smoother compared to the one of F1 and F2 (Figure 6 d, e).

3.2.3 Vp(G)

Vp(G) curves of 3 tests are presented in Figure 8. Following the literature, in the identified domain of the Vp(G) curve, the crack growth rate obeys a power law dependency on G as follows: $V_p = A.G^{\beta}$ [36, 42,43]. A and β are constants which depend on the material properties, and therefore on its formulation and thermomechanical history [41–45]. β is found equal to 2.6, 3.3, and 3.7 for F1, F2, and F3, respectively. These values are consistent with the ones found

in the literature for EPDM [20,46–49]. Vp varies from 10^{-6} m/s to 10^{-3} m/s for G values ranging from 0.4 kJ/m^2 to 2.5kJ/m^2. For practical purpose, the domain of Vp above 8.10^{-5} m/s is called hereafter high Vp or high G domain whereas the one with Vp below 8.10^{-5} m/s, low Vp or low G domain. The observed crack growth begins at low G (<0.4kJ/m^2) for both F1 and F2, whereas it is at around 0.8kJ/m^2 for F3. The high value of G for F3 may be associated to the very good dispersion of carbon black, without agglomerates. More interestingly, at the highest Vp values, G is higher for F1 than for F2.

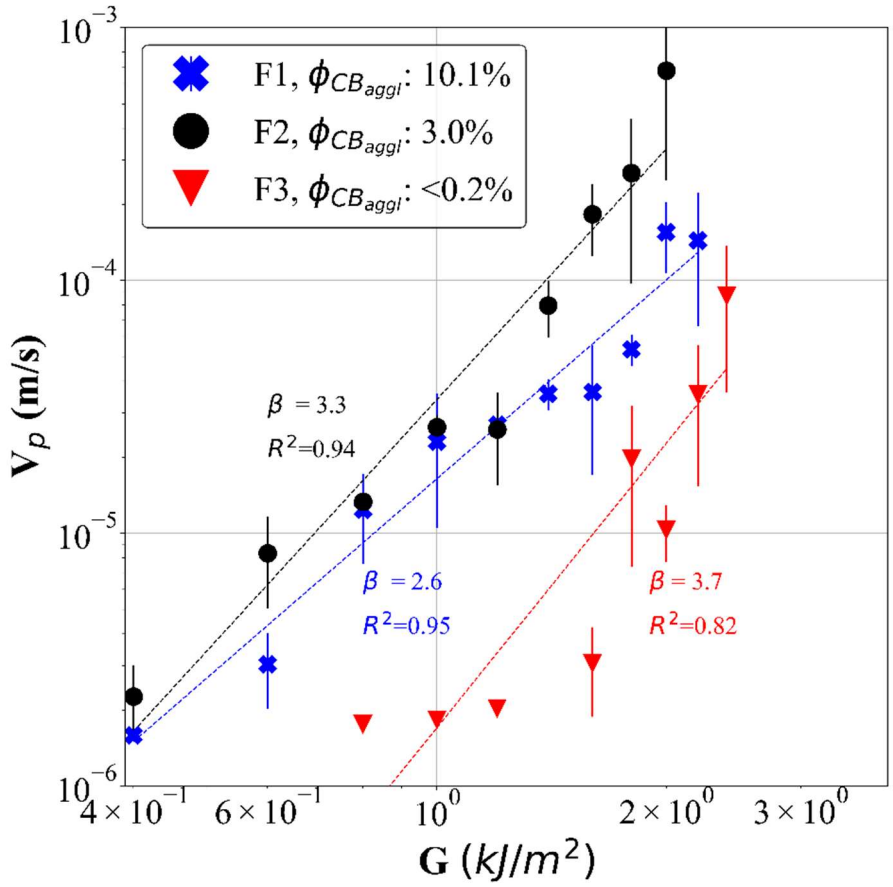

Figure 8: Vp(G) curve for F1, F2 and F3.

3.3 Microscopic analysis

3.3.1 CB_{aggl} damage mechanisms

An in-situ tensile test using SRCT (P05 imaging beamline) is used to identify local damage mechanisms at microscale. The results from F2 material are presented in Figure 9. The slice view of a CB_{aggl} at different nominal strains (Figure 9a) shows that agglomerates undergo multiple fractures. Between 40% and 50% nominal strains, we only observed the breakage of the biggest CB_{aggl} (with Eq_{diam} above ca. 78µm). For higher nominal strain, more CB_{aggl} undergo

internal fracture. The higher the nominal strain, the smaller the minimum size of the CB_{aggl} broken. For instance, the minimum Eq_{diam} of CB_{aggl} that undergoes fracture at 60% and 70% nominal strain is 33µm and 20µm respectively (Figure A6 in SI). A slice view from the 3D volume of F2 (Figure 9b) at 100% nominal strain shows that most of the agglomerates in the sample have been fractured (some are marked by a yellow circle). Moreover, the number of fractures inside a CB_{aggl} increases with the strain, as shown with the biggest observed CB_{aggl} (cf Figures 9a-b). The same phenomenon of CB_{aggl} fracture is evidenced at the crack tip in notched sample (cf. Figures 10a-d). The greyscale intensity profiles throughout the observed agglomerates at 0% and 37% nominal strain are plotted in Figure 10c and Figure 10d respectively. The minimum in the middle of the profiles is a clear indication of these fractures (marked by a circle in Figure 10*c*).

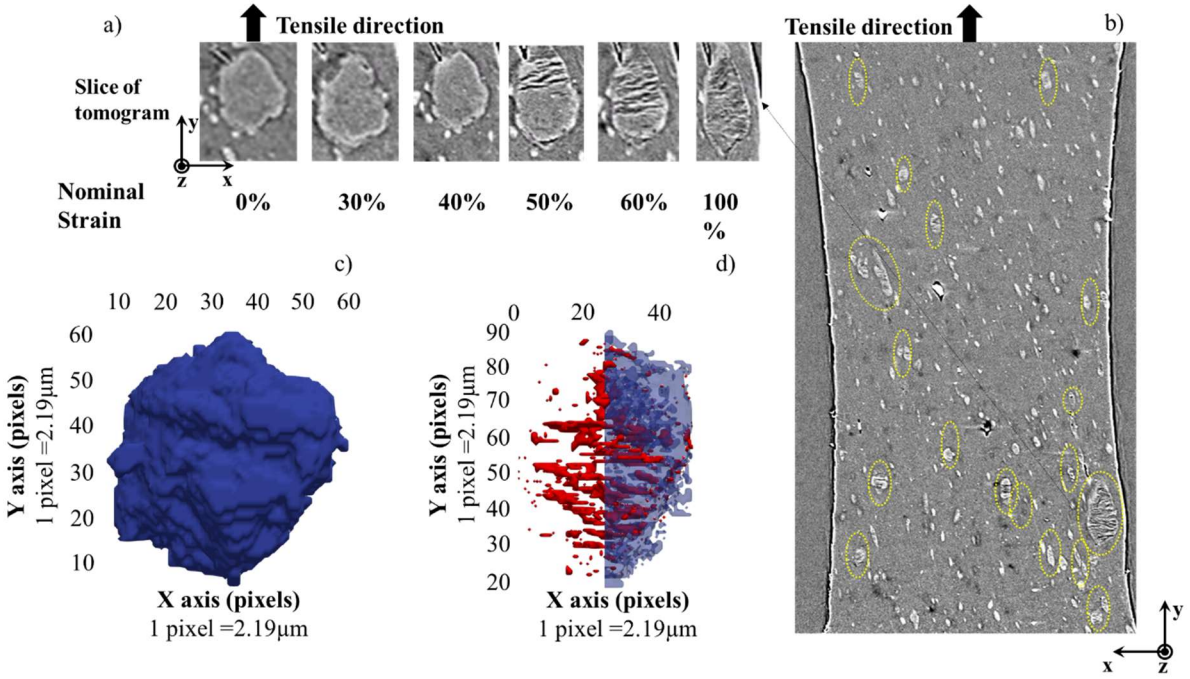

Figure 9 a) Slice view of the evolution of damage of CB_{aggl} upon stretching. b) The circles in the slice view of the sample volume at 100% nominal strain indicates the fractured agglomerates. c) and d) 3D view of the agglomerate at 0% and 100% nominal strain respectively. The red layers correspond to cavities created between the layers of fractured $CB_{aggl.}$

3.3.2 Other mechanisms observed at the crack tip

Figures 10 e)-f) and Figures 10 g)-h) present a slice view of a crack tip for F1 in two different planes, at 0% and 36% nominal strain. In the image of the first plane at 36% nominal strain (Figure 10 f), one can see that the crack has been stopped by an agglomerate. However, in the

second observation plane, for the same nominal strain, the crack has also propagated through another agglomerate (Figures 10 g)-h)). In addition, it was also observed that during crack propagation, the crack path can be sometimes deviated towards a CB_{aggl}, which was not in the initial notch plane (Figure 11). The existence of all the above mechanisms is not specific to the geometry used for SRCT, and was also confirmed with the PS geometry samples (cf. SI for further information, Description A1).

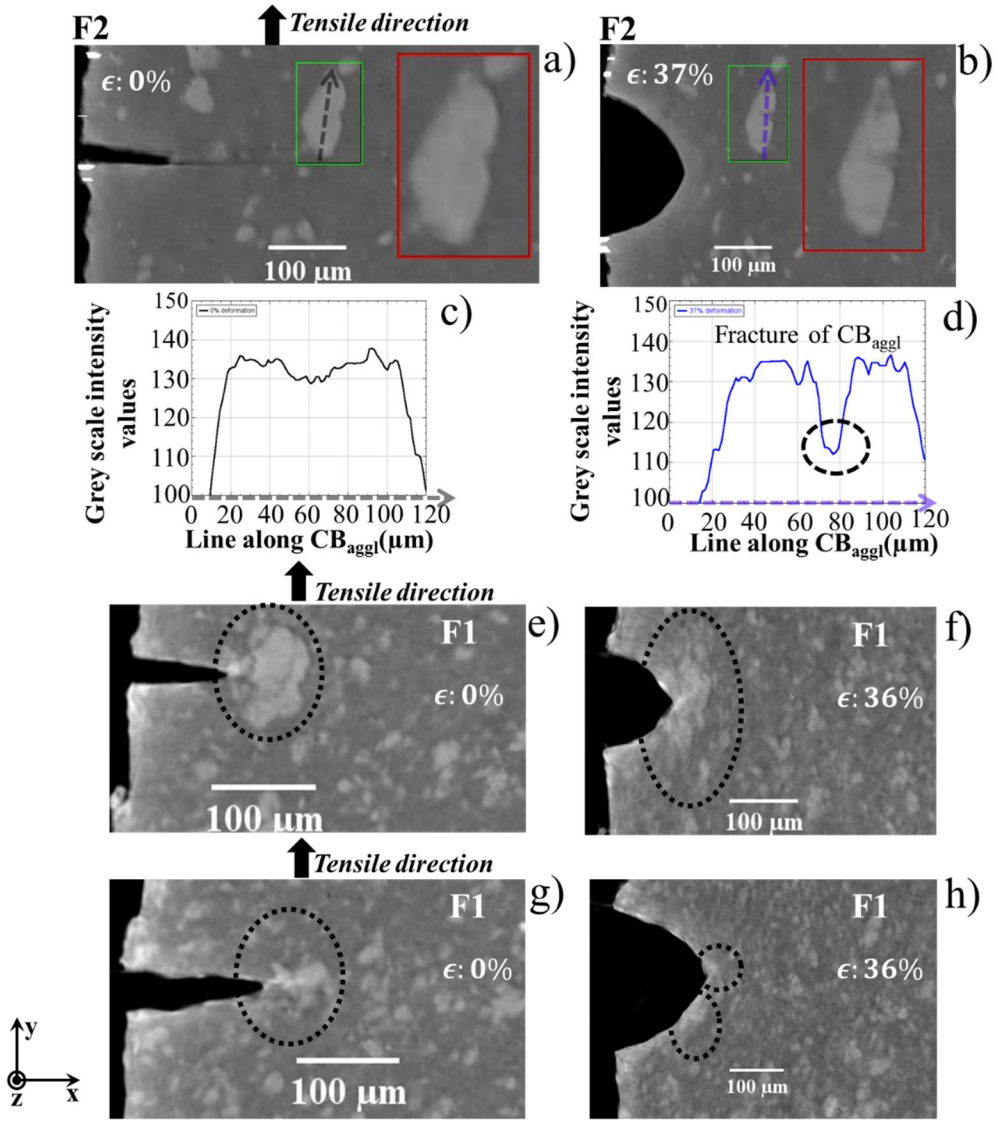

Figure 10: a)-b) Fracture of an agglomerate near a crack tip for F2 sample. c) - d) grey scale intensity values along the black and blue line drawn on the CB_{aggl} from a) and b) images respectively. e) & f) F1 material strained at 0% and 36% respectively (same observation plane). g)-h) crack propagation through a fractured agglomerate in F1 sample in another observation plane. In g) CB_{aggl} are identified by dotted circle at the crack tip. In h) the fractured CB_{aggl} is identified by 2 circles at the crack tip.

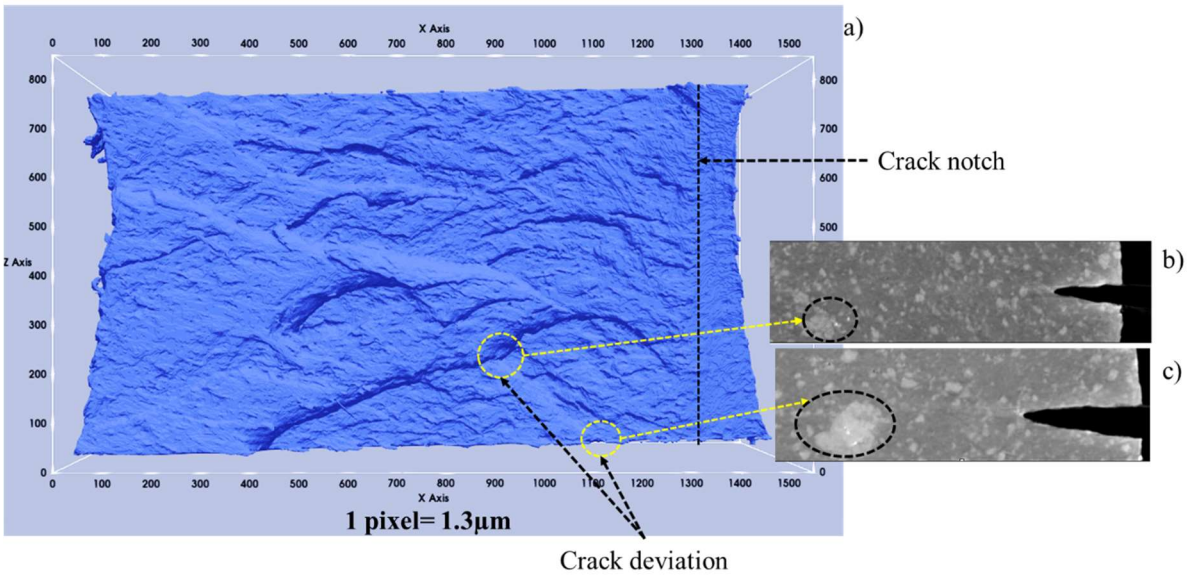

Figure 11: a) Crack surface of F1 visualized using SRCT. Crack arrests are identified by yellow circles. There is a change in the direction of crack and the crack front forms triangle waves. Post mortem analysis revealed that at each of these circled points, there was a CB_{aggl} which had stopped the propagation or deviated the crack from its original path. b)-c) The corresponding slice views of these agglomerates are presented alongside the picture (a).

4. DISCUSSION

Micron size agglomerates exist in industrial products, usually in non-negligible concentration. To understand their role on the crack propagation mechanisms, three model filled EPDM samples have been processed with a low CB_{aggl} concentration, a CB_{aggl} concentration representative of the one found commonly in industrial products, and an abnormally high one. We measured their crack propagation resistance and observed the local damage mechanisms occurring at the micron-scale during this propagation. Compared to a material with quasi absence of agglomerates (F3), increasing the agglomerates concentration to 3.0% (F2) or 10.1% (F1) does not significantly change the mechanical properties, i.e. the viscoelastic modulus and tensile stress strain curve at large strain (cf. Figure 4). Nevertheless, the crack propagation is made faster whatever the G value tested. This is consistent with the smaller curvature radius of the crack tip (SI Figure A8) and the larger maximum strain at the crack tip when they are compared to those of the F3 material (Figure 7). Our assumption is that in F1 and F2, the significant agglomerates concentration locally perturbs the material deformation at the crack tip, hence increasing the local stress concentration. More interestingly, the increase in the

agglomerates concentration from 3.0% to 10.1% decreases the crack propagation velocity as G increases.

Past studies correlated the energy dissipation during high strain loading to the crack propagation resistance[21,39,50]. Thus, the better resistance to crack propagation for filled elastomers vs unfilled one was partially attributed to an increase in the strain energy release rate, brought by the energy dissipated by the Mullins effect [16,18,50,51]. Similarly, the studies by Ducrot *et al.*[39] and Slootman[52] showed that mechanisms involving sacrificial bonds, by dissipating more energy in the crack tip vicinity, also improve the fracture toughness.

When CB_{aggl} are present, they can influence the crack propagation resistance through different mechanisms. Like in the work of reference [54], we have shown that CB agglomerates can deviate the crack from its original path (Figure 11) , and therefore increase the total crack path. In addition, they can also lead to a crack arrest as shown in Figures 10 e)-f). Thus, the crack tip is momentarily reinforced and increases the stored energy before the crack advance. Note that such mechanisms are however temporary which explains the better properties of F3 which has very few CB_{aggl}.

Moreover, we have clearly evidenced that CB_{aggl} are also the source of dissipative mechanisms. Figures 3 shows that in the 3 materials, they contain soft layers of polymer. For this reason, instead of relaxing concentration by cavitation at their poles, one observes, at sufficiently large deformation, that these CB_{aggl} do it by their internal fracture [26] (Figure 9). Such agglomerate fracture mechanisms were previously reported in the literature for materials containing silica agglomerates that has undergone fatigue[53] or quasi-static tests[8]. This is also consistent with the higher Mullins effect of the F1 material (shown by its higher ΔU_{hyst}^{n} , Figure 5) since it contains more agglomerates. Moreover, the higher the strain, the higher the energy dissipated in the big agglomerates, since those can be multi-fractured (cf. Figure 9). These mechanisms lead to more dissipated energy in F1 than in F2 (as it has a larger CB_{aggl} content), and therefore crack propagation speed (cf. Figure 8) of F1 is slower compared to F2 at large strain energy release rate. (Note that this also suggests that for a given large Vp, the strain energy release rate is higher for F1 than for F2).

Nevertheless, this does not explain the convergence of the Vp(G) curves of F1 and F2 at low G values. The size of the zone where the strain is amplified ahead of the crack tip must also be considered. Strain as a function of the distance to the crack tip, in the notch plane, is reported in Figure 12 for F1 material at low G value (0.6 kJ/m^2) and high G value (1.6 kJ/m^2) (see Figure

A9 in SI for F2). From these figures, the distance to the crack tip below which the strain is larger than 50%, 60% and 70% can be estimated. 50% is the minimum nominal strain to observe CB_{aggl} fracture. We also know the dependence of this minimum strain with the CB_{aggl} size. One can then roughly estimate the corresponding volumes in the crack tip vicinity (assuming a tube or cylindrical zone). They are reported in table A1 in SI. They indicate that a significant number of agglomerates are submitted to strain larger than the strain at which they can be fractured, confirming that a lot of agglomerates fracture are occurring ahead of the crack tip for the G domain considered. Much more agglomerates are concerned in F1 than in F2 (with a ratio around 5). Their numbers are however largely reduced when G is decreased from 1.6kJ/m^2 to 0.6kJ/m^2. Thus, we can assume that at 0.6kJ/m^2, the energy dissipated at the crack tip by the agglomerate fracture is too low in both the materials to lead to a differences in the Vp(G) curves. By increasing the G value, the dissipated energies in both the materials during crack propagation are increased as well as their difference in absolute value, hence explaining the divergence of their Vp(G) curves.

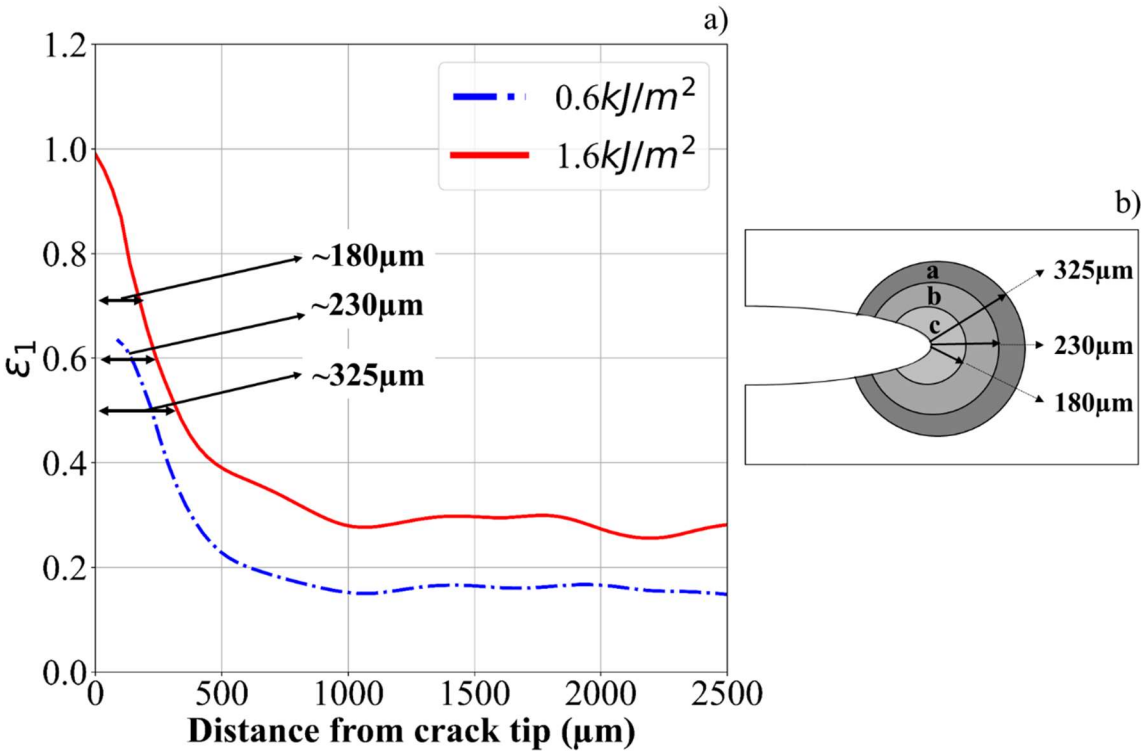

Figure 12: a) Nominal strain profile ahead of the crack tip) for F1 at 2 G values (0.6 kJ/m^2, 1.6kJ/m^2). The arrow indicates the size of the zone for which the nominal strain is above 50%, 60%, and 70%. The plot for F2 is presented in SI (Figure A9). b) Scheme of the influence zone

in F1: cylinder of radius “a” for strain between 50% and 60%, “b” for strain between 60% and 70% deformation, and “c” for strain above 70%.

5. CONCLUSION

A reinforced elastomer always contains defects such as filler agglomerates, especially when it is industrially processed. As we observed by TEM, these agglomerates are likely formed of overconcentration of filler aggregates and are therefore soft and deformable. Our original investigation by in-situ Synchrotron source X-ray tomography has showed that these agglomerates can fracture at high strain, depending on their size. Thus, they provide dissipative mechanisms around the crack tip during the crack propagation, which can be particularly significant at high strain energy release rate. Therefore, at high G, higher concentration of CB_{aggl} at the crack tip will leads to higher energy dissipation, and reduce the crack propagation speed. Apart from this mechanism, the presence of CB_{aggl} at the crack tip leads also to crack arrest or crack deviation. To conclude, this study shows that quantification of these different mechanisms is particularly important for the understanding and the prediction of crack propagation in CB filled elastomer. Of course, this can likely be generalized to all elastomers filled with nanoscopic aggregates which can form large agglomerates in the materials.

6. ACKNOWLEDGEMENTS

This work was supported by LRCCP and ANRT (CIFRE N° 2018 /0429). We thank Florent Dalmas from MATEIS, INSA Lyon who performed the TEM characterizations. Parts of this research were carried out PETRA III P05 beamline at DESY, Germany (operated by Helmholtz-Zentrum Hereon). We would like to thank the beamline staff for assistance in conducting the experiments. Some parts of the study were also carried out at ANATOMIX beamline at Soleil. ANATOMIX is an Equipment of Excellence (EQUIPEX) funded by the Investments for the Future program of the French National Research Agency (ANR), project NanoimagesX, grant no. ANR-11-EQPX-0031.

7. SUPPORTING INFORMATION

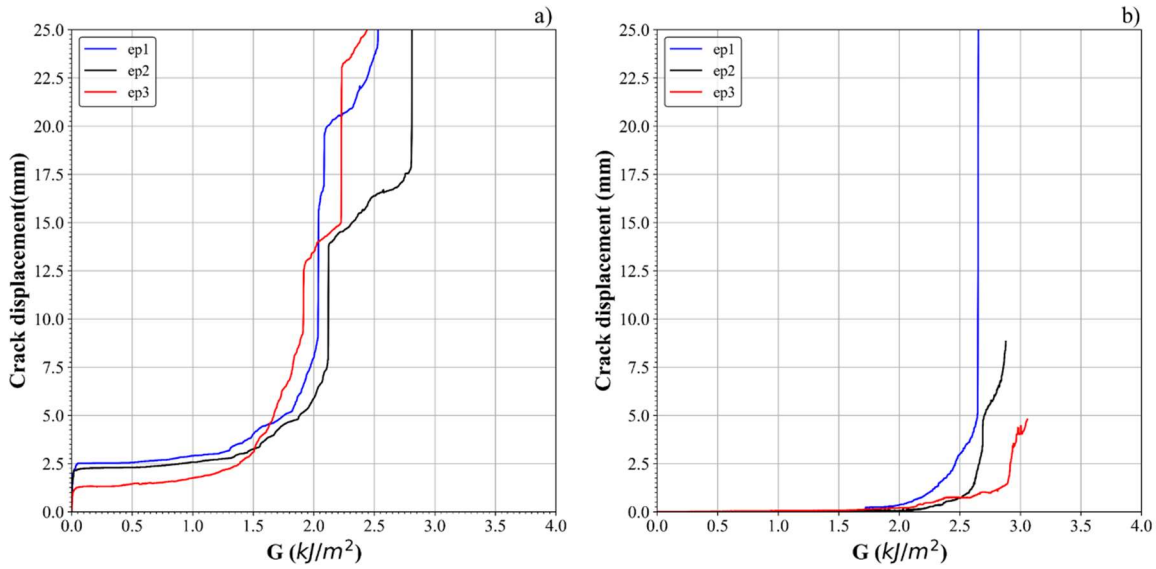

Figure A1: Crack displacement as a function of G for a) F2 and b) F3.

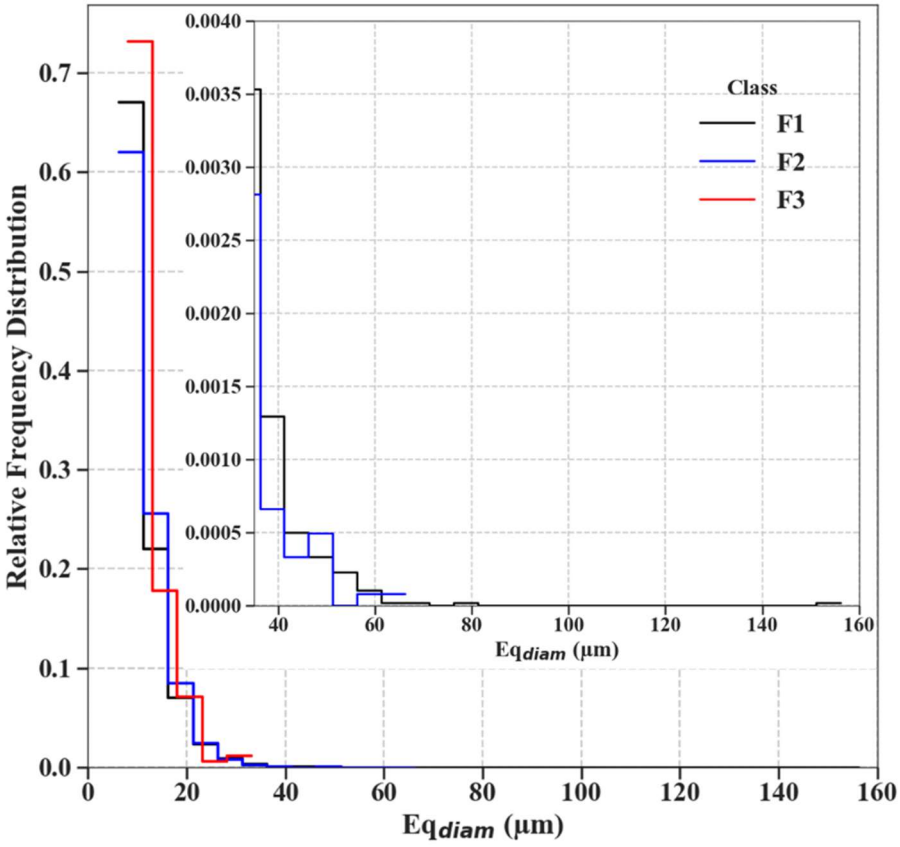

Figure A2: Distribution of the equivalent diameters of the agglomerates (Eq_{diam}) for the materials F1, F2 and F3.

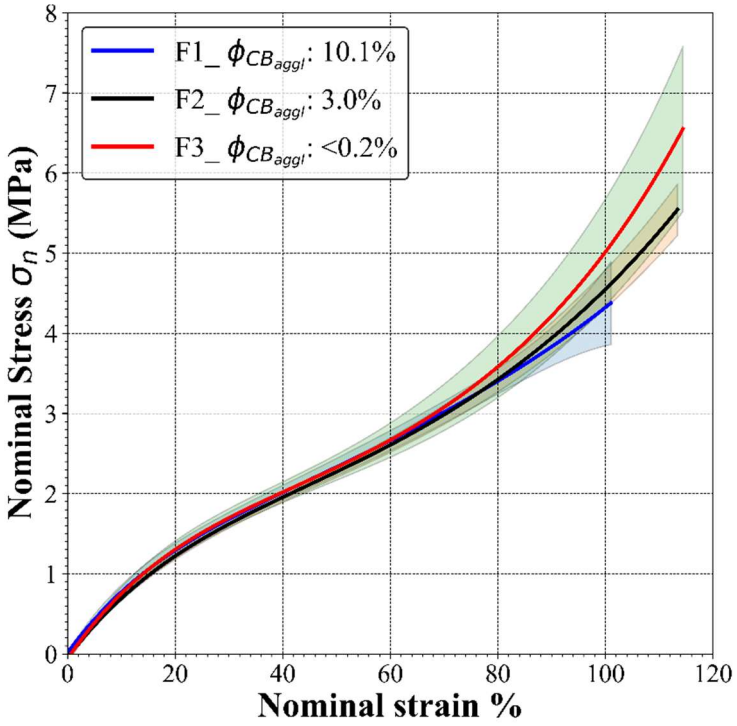

Figure A3: True Stress vs nominal strain plots of model materials using unnotched PS specimen geometry. The shaded region along each curves represents the standard deviation.

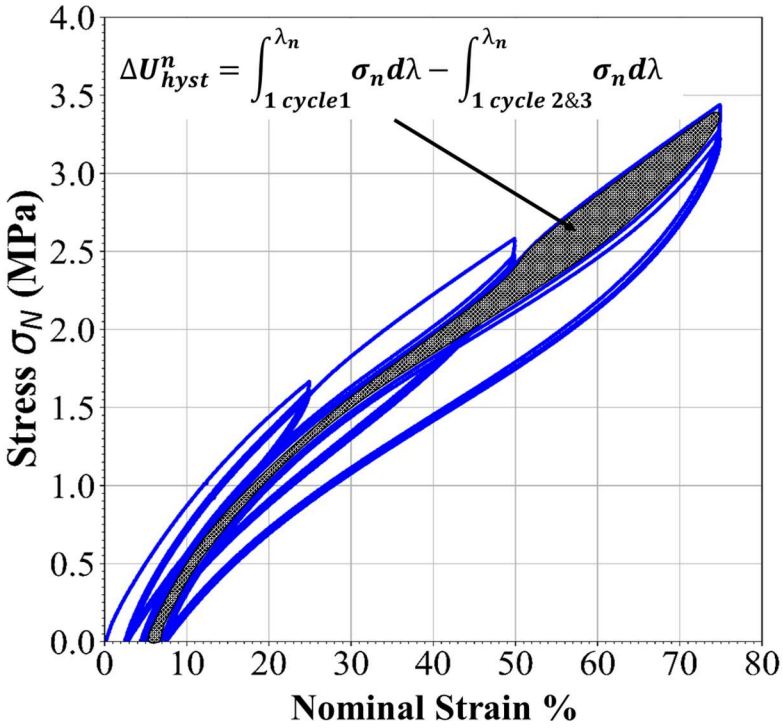

Figure A4: Materials have been cyclically deformed three times up to a fixed nominal strain

(25%, 50%, and 75%) using a dogbone sample geometry. Shaded area is the irreversible energy lost at 75% nominal strain.

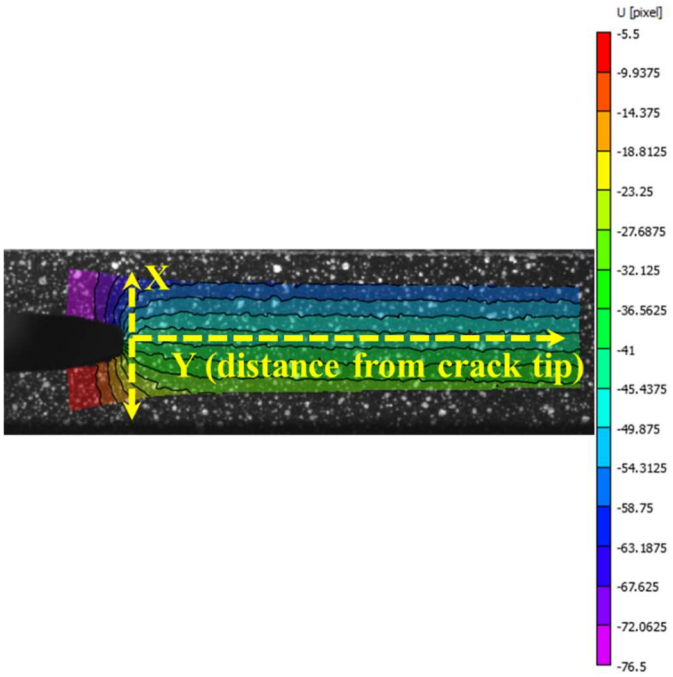

Figure A5: Example of displacement field (U_x) along the tensile direction deduced from DIC measurement during crack propagation.

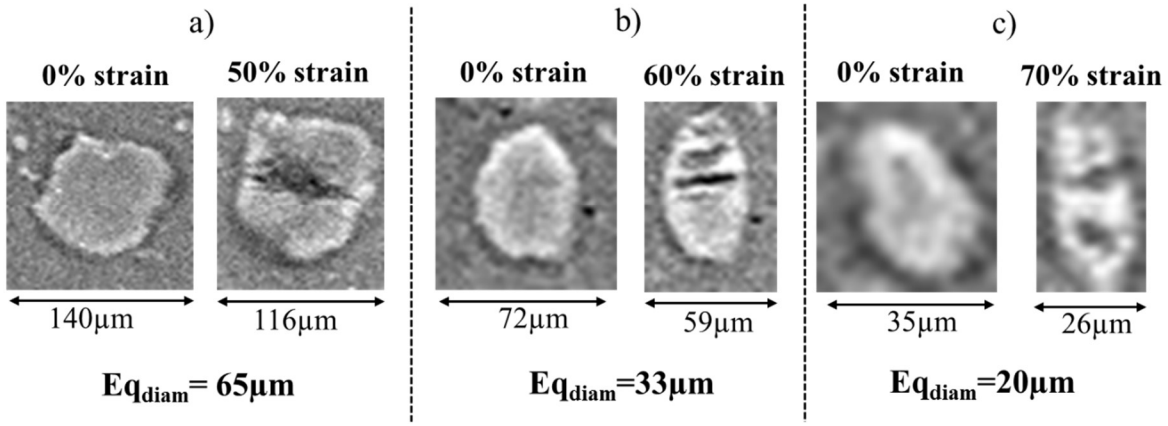

Figure A6: The smallest CB_{aggl} that undergo fracture at a given strain. a) CB_{aggl} with Eq_{diam} = 65µm undergo fracture at 50% nominal strain. b) CB_{aggl} with Eq_{diam} = 33µm undergo fracture at 50% nominal strain. c) CB_{aggl} with Eq_{diam} = 20µm undergo fracture at 50% nominal strain.

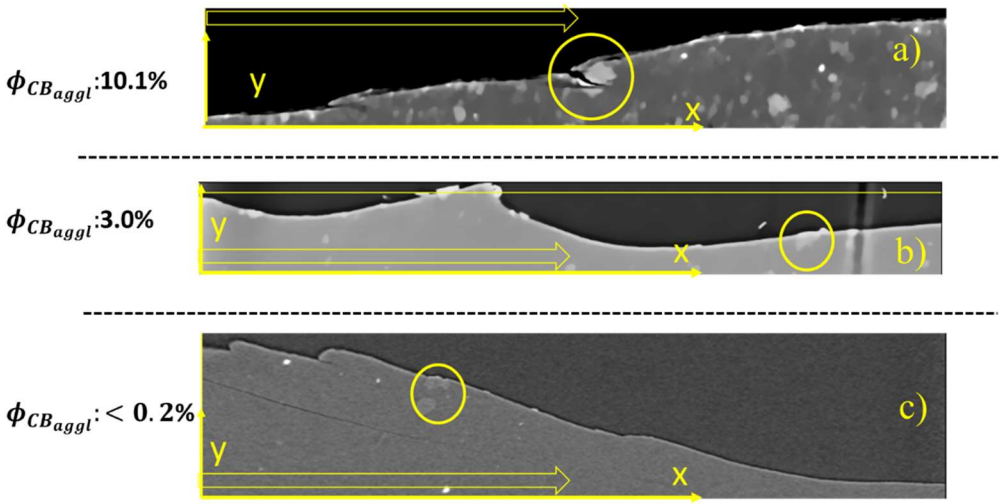

Figure A7: a)-c), slice view obtained from lab tomography of fractured surfaces for the 3 model materials. When crack approaches a CB_{aggl}, it breaks it (yellow circle) and propagates through it, rather than undergoing deviation along the agglomerate's contour, which is contrary to the mechanism often proposed in the literature[20,54]. Crack arrest is visible in F1 (yellow circle in Figure A7a) due to the presence of CB_{aggl} and a secondary crack initiation which originates from this point changes the direction of crack. Initiations of secondary crack are less observed in F2 (Figure A7b and Figure 6e). The contour of the propagation path looks similar to a saw tooth profile[21]. In F3, crack deviation is observed (visually less significant compared to F2 in Figure 6f), although it is not induced by the presence of agglomerates (Figure A7c). The crack propagation direction is modified in the very beginning, maybe due to the notch geometry. This can also be confirmed in the graph of ϵ_{max} at the crack tip for F3, as it is generally smooth throughout the crack propagation (no crack arrest).

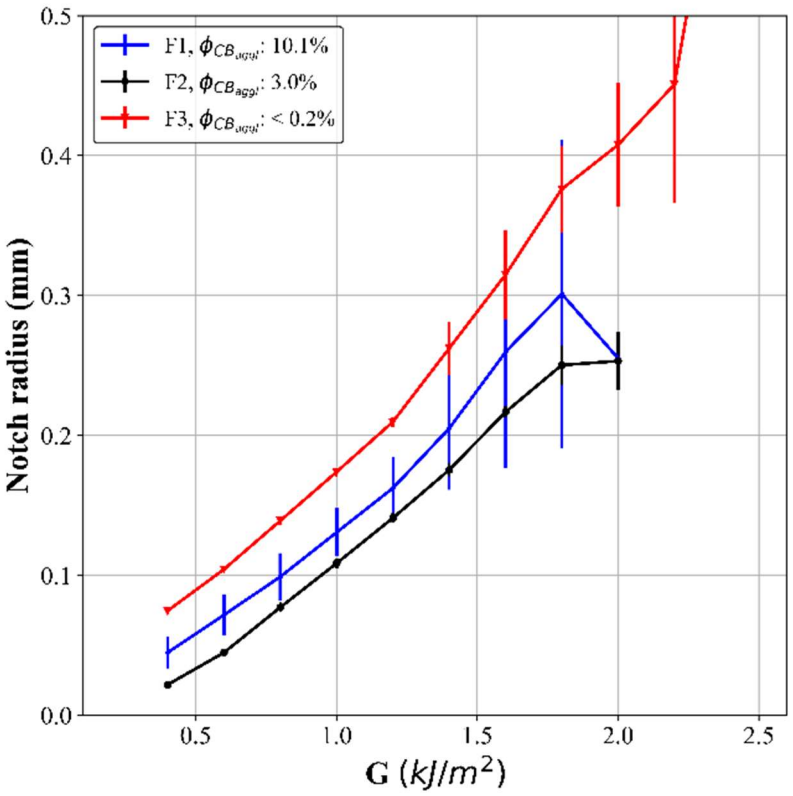

Figure A8: Evolution of notch radius as a function of G during a crack propagation in a PS (PS geometry, also called pure shear geometry in some publication, see reference [29] for a discussion about this geometry).

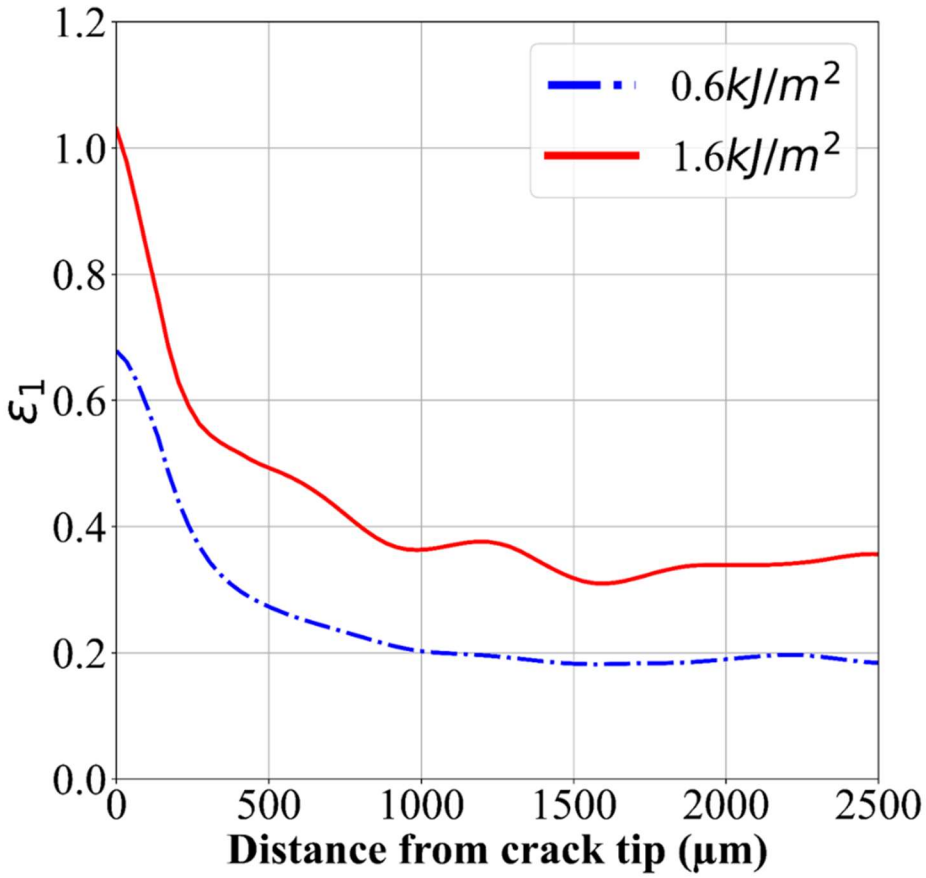

Figure A9: Nominal strain profile ahead of the crack tip in the notch plane) for F2 at 2 G values (0.6 kJ/m^2, 1.6kJ/m^2)

Calculation of Number of CB$_{aggl}$ highly deformed in the crack tip vicinity:

At 1.6 kJ/m^2 (high G), the distance from the crack tip with nominal strain greater than 50%, 60% and 70% is around 325µm, 230µm and 180µm respectively for F1. Similarly for F2, it is around 440µm, 200µm and 160µm respectively. At 0.6 kJ/m^2 (low G), size of the zone with strain above 50% and 60% for F1 is 220µm and 130µm respectively and for F2, it is 170µm and 100µm respectively. There is no zone next to the crack tip with strain greater than 70%.

Number of CB$_{aggl}$ in a zone= Volume of the zone (e.g. *a* or *b* or *c*)*volume fraction of CB$_{aggl}$/ Volume of one CB$_{aggl}$ with median Eq_{diam}

G (kJ/m^2)	Material	Zone	Length of the zone	Volume of the zone ($10^8 \mu m^3$)	Minimum size of CB_{aggl} which fracture	Median size of CB_{aggl}	Vol fraction of CB_{aggl} above the minimum size (%)	N
1.6/0.6	F1	a	325/220	1.4/0.9	65	79	0.4	2/1
		b	230/130	0.6/0.5	33	39	1.6	30/25
		c	180/-	0.9/-	20	23	4.5/0	647/0
	Total Number of CB_{aggl}							**~680/25**
	F2	a	440/170	4.3/0.3	65		0.01	0/0
		b	200/130	0.4/0.5	33	36	0.3	5/6
		c	160/-	0.3/-	20	23	1.2/-	135/0
	Total Number of CB_{aggl}							**~140/6**

Table A1: Calculation of Number of CB_{aggl} for each material in the dissipative zones

8. DATA AVAILABILITY STATEMENT

The raw/processed data required to reproduce these findings cannot be shared at this time due to technical or time limitations. They can however be provided on demand.

9. REFERENCES

[1] Medalia, A. I. Effect of Carbon Black on Ultimate Proper.Pdf *Rubber Division, Americal Chemical Society* **1986**, *60*, 45.

[2] Nusser, K.; Mosbauer, T.; Schneider, G. J.; Brandt, K.; Weidemann, G.; Goebbels, J.; Riesemeier, H.; Göritz, D. Silica dispersion in styrene butadiene rubber composites studied by synchrotron tomography *Journal of Non-Crystalline Solids* **2012**, *358*, 557, 10.1016/J.JNONCRYSOL.2011.10.009.

[3] Astruc, M. Thesis,. Étude rhéo-optique des mécanismes de dispersion de mélanges sous cisaillement simple . 1 Mélanges concentrés de polymères immiscibles . 2 Mélanges polymères-charges poreuse, l'École des Mines de Paris, **2008**.

[4] Collin, V.; Boudimbou, I.; Peuvrel-Disdier, E. New insights in dispersion mechanisms of carbon black in a polymer matrix under shear by rheo-optics *Journal of Applied Polymer Science* **2013**, *127*, 2121, 10.1002/app.37769.

[5] Dizon, E. S.; Hicks, A. E.; Chirico, V. E. The Effect of Carbon Black Parameters on the Fatigue Life of Filled Rubber Compounds. *Rubber Chem. Technol.* **1974**, *47*, 231–249.
[6] Huneau, B.; Masquelier, I.; Marco, Y.; Le Saux, V.; Noizet, S.; Schiel, C.; Charrier, P. Fatigue crack initiation in a carbon black-filled natural rubber *Rubber Chemistry and Technology* **2016**, *89*, 126, 10.5254/rct.15.84809.
[7] Le Saux, V.; Marco, Y.; Calloch, S.; Charrier, P. Evaluation of the fatigue defect population in an elastomer using X-ray computed micro-tomography *Polymer Engineering & Science* **2011**, *51*, 1253, 10.1002/pen.21872.
[8] Federico, C. E.; Padmanathan, H. R.; Kotecký, O.; Rommel, R.; Rauchs, G.; Fleming, Y.; Addiego, F. Resolving cavitation in silica-filled styrene-butadiene rubber composites upon cyclic tensile testing *Polymer Testing* **2021**, *100*, 107274, 10.1016/j.polymertesting.2021.107274.
[9] Gent, A. N.; Park, B. Failure processes in elastomers at or near a rigid spherical inclusion *Journal of Materials Science* **1984**, *19*, 1947, 10.1007/BF00550265.
[10] Poulain, X.; Lefèvre, V.; Lopez-Pamies, O.; Ravi-Chandar, K. Damage in elastomers: nucleation and growth of cavities, micro-cracks, and macro-cracks *International Journal of Fracture* **2017**, *205*, 10.1007/s10704-016-0176-9.
[11] Beurrot, S.; Huneau, B.; Verron, E. In situ SEM study of fatigue crack growth mechanism in carbon black-filled natural rubber *Journal of Applied Polymer Science* **2010**, *43*, NA, 10.1002/app.31707.
[12] Le Cam, J. B.; Huneau, B.; Verron, E.; Gornet, L. Mechanism of fatigue crack growth in carbon black filled natural rubber *Macromolecules* **2004**, *37*, 5011, 10.1021/ma0495386.
[13] Aglan, H.; Chudnovsky, A.; Moet, A.; Fleischman, T.; Stalnaker, D. Crack layer analysis of fatigue crack propagation in rubber compounds *International Journal of Fracture* **1990**, *44*, 167, https://doi.org/10.1007/BF00035514.
[14] Saintier, N. Thesis,. Fatigue multiaxiale dans un élastomère de type NR chargé : mécanismes d'endommagment et critère local d'amorçage de fissure, Ecole Nationale Supérieure d'Arts et Métiers, **2001**.
[15] Roland, C. M.; Smith, C. R. Defect Accumulation in Rubber. *Rubber Chem. Technol.* **1985**, *58*, 806–814.
[16] Tsunoda, K.; Busfield, J. J. C.; Davies, C. K. L.; Thomas, A. G. Effect of materials variables on the tear behaviour of a non-crystallizing elastomer *Journal of Materials Science* **2000**, *35*, 5187, 10.1023/A:1004860522186.
[17] Oberth, A. E.; Bruenner, R. S. Tear Phenomena around Solid Inclusions in Castable Elastomers *Transactions of the Society of Rheology* **1965**, *9*, 165, 10.1122/1.548997.
[18] Fukahori, Y.; Sakulkaew, K.; Busfield, J. J. C. Elastic-viscous transition in tear fracture of rubbers *Polymer* **2013**, *54*, 1905, 10.1016/j.polymer.2013.01.019.
[19] Kraus, G. Reinforcement of elastomers by carbon black; In *Fortschritte der Hochpolymeren-Forschung*; Springer Berlin Heidelberg: Berlin, Heidelberg; pp 155; 10.1007/3-540-05483-9_12.
[20] Lorenz, H.; Steinhauser, D.; Klüppel, M. Morphology and Micro-mechanics of Filled Elastomer Blends: Impact on Dynamic Crack Propagation; **2013**; pp 81; 10.1007/978-3-642-37910-9_3.
[21] Stacer, R. G.; Yanyo, L. C.; Kelley, F. N. Observations on the Tearing of Elastomers. *Rubber Chem. Technol.* **1985**, *58*, 421–435.
[22] Le Cam, J.-B.; Huneau, B.; Verron, E. Fatigue damage in carbon black filled natural rubber under uni- and multiaxial loading conditions *International Journal of Fatigue* **2013**, *52*, 82, 10.1016/j.ijfatigue.2013.02.022.

[23] Pal, P. K.; Bhowmick, A. K.; De, S. K. Scanning Electron Microscopy Studies on Failure of Natural Rubber. *Int. J. Polym. Mater. Polym. Biomater.* **1982**, *9*, 139–149.
[24] Zhang, F.; Chen, Y.; Sun, C.; Wen, S.; Liu, L. Network evolutions in both pure and silica-filled natural rubbers during cyclic shear loading *RSC Advances* **2014**, *4*, 26706, 10.1039/c4ra02003k.
[25] Mdarhri, A.; Elies, P.; Brosseau, C. Stress induced cracks in carbon black filled elastomers probed by atomic force microscopy *Journal of Applied Physics* **2008**, *104*, 10.1063/1.3042218.
[26] Cao, X.; Zhou, X.; Weng, G. Nanocavitation in silica filled styrene-butadiene rubber regulated by varying silica-rubber interfacial bonding *Polymers for Advanced Technologies* **2018**, *29*, 1779, 10.1002/pat.4284.
[27] Maire, E.; Withers, P. J. Quantitative X-ray tomography *International Materials Reviews* **2014**, *59*, 1, 10.1179/1743280413Y.0000000023.
[28] Withers, P. J. Fracture mechanics by three-dimensional crack-tip synchrotron X-ray microscopy *Philosophical Transactions of the Royal Society A: Mathematical, Physical and Engineering Sciences* **2015**, *373*, 10.1098/rsta.2013.0157.
[29] Buffière, J.-Y.; Maire, E. *Imagerie 3D en mécanique des matériaux*; Hermes Science Publications, Ed.; Lavosier, **2014**.
[30] Maire, E.; Le Bourlot, C.; Adrien, J.; Mortensen, A.; Mokso, R. 20 Hz X-ray tomography during an in situ tensile test *International Journal of Fracture* **2016**, *200*, 3, 10.1007/s10704-016-0077-y.
[31] Stoček, R.; Stěnička, M.; Maloch, J. Determining Parametrical Functions Defining the Deformations of a Plane Strain Tensile Rubber Sample; **2020**; pp 19; 10.1007/12_2020_78.
[32] Kallungal, J.; Chazeau, L.; Chenal, J.-M.; Adrien, J.; Maire, E.; Barres, C.; Cantaloube, B.; Heuillet, P. Methodology for 3D characterization of microstructural defects in filled polymer using X-ray Tomography; In *Constitutive Models for Rubber XI*; CRC Press, **2019**; pp 77; 10.1201/9780429324710-14.
[33] Weitkamp, T.; Scheel, M.; Perrin, J.; Daniel, G.; King, A.; Le Roux, V.; Giorgetta, J.-L.; Carcy, A.; Langlois, F.; Desjardins, K.; Menneglier, C.; Cerato, M.; Engblom, C.; Cauchon, G.; Moreno, T.; Rivard, C.; Gohon, Y.; Polack, F. Microtomography on the ANATOMIX beamline at Synchrotron SOLEIL; In *14th International Conference on Synchrotron Radiation Instrumentation (SRI 2021)*; J. Phys. Conf., **2022**; in press.
[34] Paganin, D.; Mayo, S. C.; Gureyev, T. E.; Miller, P. R.; Wilkins, S. W. Simultaneous phase and amplitude extraction from a single defocused image of a homogeneous object *Journal of Microscopy* **2002**, *206*, 33, 10.1046/j.1365-2818.2002.01010.x.
[35] Rivlin, R. S.; Thomas, A. G. Rupture of rubber. I. Characteristic energy for tearing *Journal of Polymer Science* **1953**, *10*, 291, 10.1002/pol.1953.120100303.
[36] Lake, G. J.; Lawrence, C. C.; Thomas, A. G. High-speed fracture of elastomers: Part I *Rubber Chemistry and Technology* **2000**, *73*, 801, 10.5254/1.3547620.
[37] Yeoh, O. H. Fracture mechanics of bond failure in the "pure shear" test piece *Rubber Chemistry and Technology* **2003**, *76*, 483, 10.5254/1.3547755.
[38] van der Walt, S.; Schönberger, J. L.; Nunez-Iglesias, J.; Boulogne, F.; Warner, J. D.; Yager, N.; Gouillart, E.; Yu, T. scikit-image: image processing in Python *PeerJ* **2014**, *2*, e453, 10.7717/peerj.453.
[39] Ducrot, E.; Chen, Y.; Bulters, M.; Sijbesma, R. P.; Creton, C. Toughening Elastomers with Sacrificial Bonds and Watching Them Break *Science* **2014**, *344*, 186, 10.1126/science.1248494.
[40] Papadopoulos, I. C.; Thomas, A. G.; Busfield, J. J. C. Rate transitions in the fatigue crack growth of elastomers *Journal of Applied Polymer Science* **2008**, *109*, 1900,

10.1002/app.28086.
[41] Kaang, S.; Jin, Y. W.; Huh, Y. il; Lee, W. J.; Im, W. Bin A test method to measure fatigue crack growth rate of rubbery materials *Polymer Testing* **2006**, *25*, 347, 10.1016/j.polymertesting.2005.12.005.
[42] Gent, A. N.; Lindley, P. B.; Thomas, A. G. Cut growth and fatigue of rubbers. I. The relationship between cut growth and fatigue *Journal of Applied Polymer Science* **1964**, *8*, 455, 10.1002/app.1964.070080129.
[43] Lake, G. J.; Lindley, P. B. Cut growth and fatigue of rubbers. II. Experiments on a noncrystallizing rubber *Journal of Applied Polymer Science* **1964**, *8*, 707, 10.1002/app.1964.070080212.
[44] Grasland, F. Thesis,. Vieillissement du caoutchouc naturel parthermo-oxydation: Etudes de ses conséquences sur lacristallisation sous déformation, la fissuration et larupture, INSA Lyon, **2018**.
[45] Grasland, F.; Chazeau, L.; Chenal, J.-M.; Caillard, J.; Schach, R. About the elongation at break of unfilled natural rubber elastomers *Polymer* **2019**, *169*, 195, 10.1016/j.polymer.2019.02.032.
[46] Stoček, R. Some Revisions of Fatigue Crack Growth Characteristics of Rubber; **2020**; pp 1; 10.1007/12_2020_72.
[47] Klüppel, M. The role of filler networking in fatigue crack propagation of elastomers under high-severity conditions *Macromolecular Materials and Engineering* **2009**, *294*, 130, 10.1002/mame.200800263.
[48] Klüppel, M. Evaluation of viscoelastic master curves of filled elastomers and applications to fracture mechanics *Journal of Physics Condensed Matter* **2009**, *21*, 10.1088/0953-8984/21/3/035104.
[49] Stoček R., Heinrich G., Gehde M., K. R. Analysis of Dynamic Crack Propagation in Elastomers by Simultaneous Tensile- and Pure-Shear-Mode Testing.; In *Fracture Mechanics and Statistical Mechanics of Reinforced Elastomeric Blends.*; Grellmann W., Heinrich G., Kaliske M., Klüppel M., Schneider K., V. T., Ed.; Springer, Berlin, Heidelberg: vol 70., **2013**; pp 269; https://doi.org/10.1007/978-3-642-37910-9_7.
[50] Lake, G. J.; Thomas, A. G. The strength of highly elastic materials *Proceedings of the Royal Society of London. Series A. Mathematical and Physical Sciences* **1967**, *300*, 108, 10.1098/rspa.1967.0160.
[51] Chazeau, L.; Chenal, J.-M.; Gauthier, C.; Kallungal, J.; Caillard, J. About the Influence of Materials Parameters on the Ultimate and Fatigue Properties of Elastomers; In *Fatigue Crack Growth in Rubber Materials. Advances in Polymer Science*; G., H.; R., K.; R., S., Eds.; Springer, Cham., **2020**; pp 297; 10.1007/12_2020_80.
[52] Slootman, J. Thesis,. Quantitative detection of damage in soft materials using mechano-fluorescence, l'Ecole Supérieure de Physique et de Chimie Industrielles de la ville de Paris (ESPCI Paris), **2019**.
[53] Le Saux, V.; Marco, Y.; Calloch, S.; Charrier, P. Evaluation of the fatigue defect population in an elastomer using X-ray computed micro-tomography *Polymer Engineering & Science* **2011**, *51*, 1253, 10.1002/pen.21872.
[54] Jajam, K. C.; Tippur, H. V. Role of inclusion stiffness and interfacial strength on dynamic matrix crack growth: An experimental study *International Journal of Solids and Structures* **2012**, *49*, 1127, 10.1016/j.ijsolstr.2012.01.009.